JOURNAL OF GEOPHYSICAL RESEARCH, VOL. 90, NO. B1, PAGES 592–604, JANUARY 10, 1985

Forecast Model for Moderate Earthquakes Near Parkfield, California

WILLIAM D. STUART

U.S. Geological Survey, Pasadena, California
Department of Geological Sciences, Case Western Reserve University, Cleveland, Ohio

RALPH J. ARCHULETA[1] AND ALLAN G. LINDH

U.S. Geological Survey, Menlo Park, California

Earthquake instability models have possible application to earthquake forecasting because the models simulate both preseismic and coseismic changes of fault slip and ground deformation. In the forecast procedure proposed here, repeated measurements of preseismic fault slip and ground deformation constrain the values of model parameters. The early part of the model simulation corresponds to the available field data, and the subsequent part constitutes an estimate of future faulting and ground deformation. In particular, the time, location, and size of unstable faulting are estimates of the pending earthquake parameters. The forecast accuracy depends on the model realism and parameter resolution. The forecast procedure is applied to fault creep and trilateration data measured near Parkfield, California, where at least five magnitude 5.5 to 6 earthquakes have occurred regularly since 1881, the last in 1966. The quasi-static model consists of a flat vertical plane embedded in an elastic half space. Spacially variable fault slip of strike-slip sense is driven by an increasing regional shear stress but is impeded by a relatively strong patch of brittle, strain-softening fault. The field data are consistent with these approximate values of patch parameters: radius of 3 km, patch center 5 km deep and 8 km southeast of the 1966 epicenter, and maximum brittle strength of 26 bars. Fluctuations in the available field data prevent estimating the earthquake time with any more precision than use of the 21 ± 8 year recurrence interval. However, the model may later give a more precise estimate of the earthquake time if the fault slip rate near the inferred patch increases before the earthquake, as predicted by the model.

INTRODUCTION

Current methods for using time-dependent geophysical data to estimate the time of a future earthquake fall into two groups. Methods of the first group relate the earthquake time to the time of trend changes in data, for example, rate increases of seismicity, radon emanation, or ground deformation. Methods of the second group relate the earthquake time to proximity of some measure of fault stress or slip deficit to a critical value. Although several of these methods appear to have led to a few successful predictions, none have proved to be generally reliable. The reasons for the limited success are unclear but probably include uncertain relation between the observations and the earthquake-generating process, inappropriate choices of trend changes or critical values, and sparse and imprecise observations.

We propose another forecast method which combines a theoretical mechanical model for earthquake instability [e.g., *Rice*, 1980; *Stuart*, 1979*a*] with repeated measurements of ground deformation made before the earthquake. The method exploits the fact that instability models, unlike conventional strain accumulation models, simulate both slow aseismic faulting before an earthquake and the sudden fault slip during an earthquake. The essence of the method is the adjustment of model parameter values so that the observed deformation versus time curves match the appropriate preinstability section of theoretical curves provided by the simulation. The continuation of the theoretical curves, corresponding to future times, is equivalent to a prediction of ground deformation. The time of instability, if instability is possible, is an estimate of the earthquake time. Said differently, the instability model provides curves for extrapolating observed ground deformation into the future. The forecast accuracy will depend on the accuracy (physical realism) of the mathematical model and the ability of field measurements to resolve the model parameters. To be accurate, the model must adequately represent the geometry and constitutive properties of each field area where a forecast is to be attempted. This strategy, of course, is just the faulting analog of numerical methods for weather forecasting in which synoptic data are the initial conditions for time integration of the equations describing atmospheric flow.

We apply the procedure to attempt a forecast of the next moderate ($M_L = 5.5$–6) earthquake on the San Andreas fault near Parkfield, California. Parkfield is well suited for testing the procedure for three reasons. First, the fault geometry is well known from surface mapping [*Brown*, 1970], fault creep measurements [*Schulz et al.*, 1982], and seismicity distribution [*Buhr and Lindh*, 1982]. Second, according to *Bakun and McEvilly* [1979, 1984], at least five earthquakes of similar magnitude and epicenter have occurred at 21 ± 8 year intervals (1881, 1901, 1922, 1934, 1966), and, by extrapolation, the next is due about 1987. Third, because of the 1966 earthquake and anticipation of the next one, the Parkfield area has become heavily instrumented for geodetic and seismological measurements. With available data, the proposed forecast procedure cannot reduce the uncertainty of the 1987 date, but the model predicts detectable accelerating fault slip and ground deformation starting about one year before the next earthquake. At that time the procedure may give a more precise estimate of the earthquake time than use of the recurrence interval alone.

We note that earthquake instability models are consistent with principles of mechanics and in broad agreement with the

[1]Now at Department of Geological Sciences, University of California, Santa Barbara.

Paper number 4B1214.
0148-0227/85/004B-1214$05.00

main observed features of seismic and aseismic faulting but that only one model has been tested with ground deformation data associated with a specific earthquake. In that study, *Stuart* [1979*b*] found that the theoretical ground uplift agreed with uplift observed during the 6 years before the 1971 San Fernando, California, earthquake, a magnitude 6.4 event. Thus the analysis in this paper should be viewed as both a partial test of a particular strain-weakening instability model and as an application of the model to earthquake forecasting.

INSTABILITY MODEL

Qualitative Model

We first describe a qualitative version of the instability model, briefly justifying its features with field data and theoretical results, and then present the boundary value problem. The qualitative model, shown in Figure 1, is essentially the model of *Wesson et al.* [1973], though they did not consider instability explicitly or pose and solve a boundary value problem. In its mathematical form, the model is a generalization to three dimensions of two-dimensional models for unstable slip on vertical strike-slip faults [*Stuart and Mavko*, 1979] and dipping thrust faults [*Stuart*, 1979*b*]. The fault zone, represented by a flat vertical plane of discontinuous displacement, is assumed to be made of brittle areas or patches of relatively high strength rock surrounded by weaker intervening areas. The remaining crust, represented by an elastic half space, transmits the remotely applied shear stress τ^r, which approximates regional forces that increase with time. The regional stress τ^r causes the weak portions of the fault to slip, but, at least initially, the strong patches resist slippage. Both τ^r and the dislocation stress caused by fault slip load the patches and cause the half space and its surface to deform. Recurring unstable failures of the middle patch produce moderate earthquakes like the 1966 event and its predecessors.

The much longer lobe-shaped patch on the right in Figure 1 is assumed to be so strong that the fault is effectively locked. This assumption is consistent with fault creep and geodetic data [*Slawson and Savage*, 1983] which indicate that this section of fault has not slipped since the 1857 Fort Tejon earthquake, a magnitude 8.3 event [*Sieh*, 1978]. Thus the right patch is locked for the model simulation, and the model does not allow for failure of the middle patch inducing failure of the right patch. In a more general instability model, failure of the right patch could produce large earthquakes such as the 1857 earthquake. Smaller patches like the one on the left at the 1966 focus may exist as well but cannot be located with any confidence. Under increasing τ^r, patches for moderate earthquakes initially impede the southward flow of vertical edge dislocations on the San Andreas fault. When the patches fail, the dislocation pileups advance to or perhaps a few kilometers into the 1857 locked section. Alternatively, one can think of the creeping section north of Parkfield as a stress-free crack whose southern tip periodically advances and retreats.

We show below that the location and size of the middle patch are consistent with the relatively low rates of nearby fault creep and lengthening of a trilateration line measured after 1970. The patch also coincides with the location of maximum slip during the 1966 earthquake, in agreement with the computed result that unstable slip is maximum near the patch center.

Seismicity patterns on the fault may also be interpreted as being consistent with the same patch location and geometry, though the arguments are less persuasive because the mathematical model does not produce the numerous small instabilities corresponding to small earthquakes. Figure 2 shows a projection onto the fault plane of foci of $M_L > 1.5$ earthquakes occurring within 5 km of the fault between 1975 and 1980. Hypocenters are determined by the master event method and are accurate to about 0.5 km in horizontal directions and 1 km in the vertical direction. The patch boundaries, the same as in Figure 1, are reconciled with seismicity by supposing that within patches, where the fault is strong, seismicity is relatively low, but near patch boundaries, where strain rates are high owing to dislocation pileup, the seismicity is higher. Nearly continuous ductile faulting below 10 to 15 km is implied by geodetic data and the lack of seismicity [*Slawson and Savage*, 1983]. The high seismicity near the focus of the 1966 mainshock and its foreshock ($M_L = 5.1$ [*Bakun and McEvilly*, 1981]) may be due to the small patch shown on the left in Figure 1. However, small patches at the 1966 hypocenter and elsewhere are not resolvable by the creep and trilateration data, which are the main constraints on model parameters, and therefore are not included in the mathematical model.

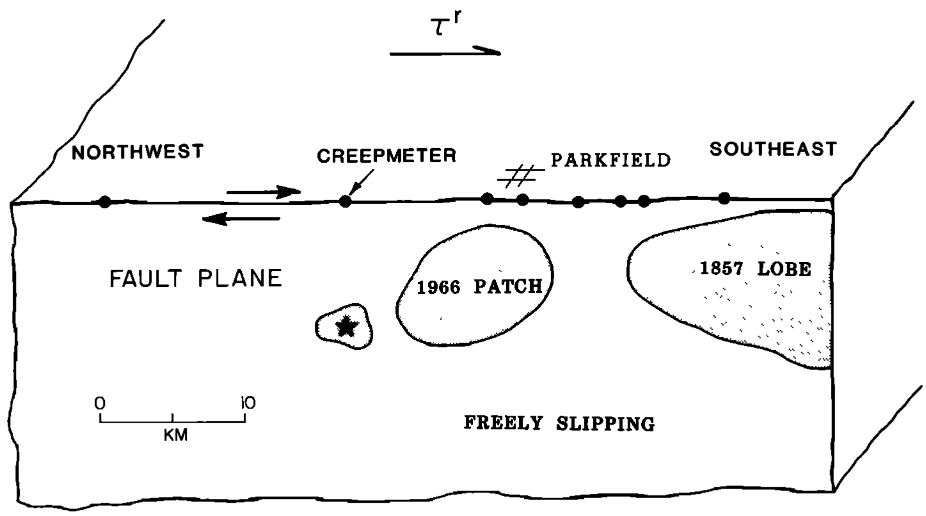

Fig. 1. Sketch of instability model with three brittle patches (shaded) of relatively high strength. Failure of the middle patch produces $M_L = 5.5$–6 earthquakes; failure of the right patch produces less frequent larger earthquakes. Small patch on left possibly associated with focus (star) of $M_L = 5.5$–6 earthquakes. τ^r represents increasing regional shear stress.

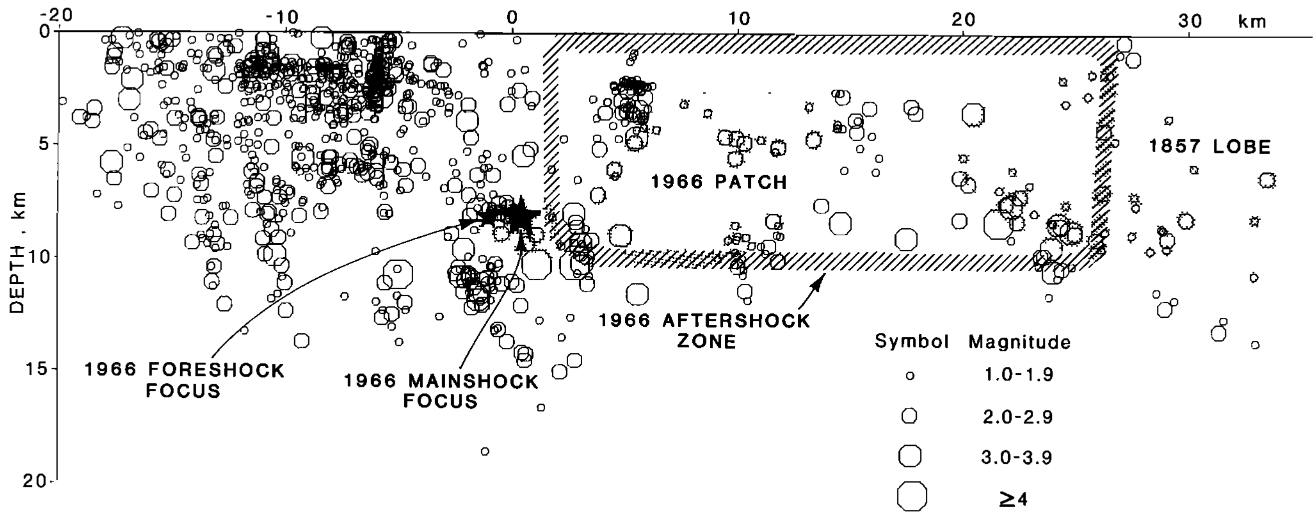

Fig. 2. Seismicity on the San Andreas fault near Parkfield from 1975–1980, $M_L > 1.5$. Hypocenters of 1966 mainshock and foreshock shown by large and small stars. Hachured band encloses aftershocks of the 1966 mainshock. Patches of Figure 1 indicated by shaded areas.

Boundary Value Problem

We now consider the fault geometry, the patch stress-slip law, instability, and fault stress equilibrium of the mathematical model. Figure 3*a* shows the surface trace of the model fault plane (x-z plane), the mapped trace of the San Andreas fault, the 1966 mainshock epicenter, and locations of creepmeters and trilateration lines. Figure 3*b* shows the fault plane, the strength contours of the slip-softening patch, areas of freely slipping fault, and the locked fault (hachured). The locked lobe on the right corresponds to the right patch in Figures 1 and 2. The three other locked boundaries are required for numerical solution. The boundary at $x = -90$ km is near the northwest end of the creeping section of the San Andreas fault. The boundary at $x = 90$ km is northwest of the major eastward bend of the San Andreas fault. The boundary at $z = 54$ km is poorly constrained by field data and is merely chosen to be far from the large strain gradients at the patch and lobe.

The assumed stress-slip law of the patch has two parts, one for the slip dependence of shear stress at specified positions on the patch, and the other for the spacial variation of patch strength. At each position on the patch, the shear stress that resists fault slip is assumed to initially increase with fault slip (slip hardening) up to a peak stress (strength or upper yield stress), then decrease with continued slip (slip softening or failure) down to the lower yield stress. Such stress-slip curves composed of positive and negative slope segments are characteristic of deformation of brittle rock (cf. *Jaeger and Cook* [1979, section 4.2]).

The peak stress of the patch is assumed to vary on the fault plane such that the strength is maximum at the patch center and decreases smoothly with distance from the center. At a sufficiently large distance from the patch center, the peak stress is negligible and the fault slips freely at the lower yield stress regardless of the slip amount.

A simple analytical form that has the above properties is

$$\tau^f = S \exp\left[-\left(\frac{x-x_0}{a_x}\right)^2\right] \exp\left[-\left(\frac{z-z_0}{a_z}\right)^2\right] \cdot \exp\left[-\left(\frac{u}{a_u}\right)^2\right] \qquad (1)$$

where τ^f is shear stress τ_{yx} that resists fault slip u, S is maximum peak stress which occurs at the patch center (x_0, z_0), and a_x and a_z are characteristic patch radii in the x and z directions. The first two Gaussian terms in (1) multiplied by S describe the variation of peak stress with position; $a_x > a_z$ corresponds to a patch elongated along strike. The last Gaussian term in (1) describes the initial slip hardening ($u < 0$) and subsequent slip softening ($u > 0$) of the fault at a position (x, y) on the fault; a_u is a characteristic slip during which the fault stress drops by S during failure. There is no loss of generality in defining the origin for the u axis to be at the peak stress because other origins correspond to adding a constant to the regional stress.

In later discussion it will be convenient to describe shrinkage of the patch in terms of motion of the patch edge. The edge is defined to be the locus of points on the fault where $u = 0$, i.e., where the patch is at peak stress. Where $u < 0$, the patch is unfailed, and where $u > 0$, the patch is failing or has already failed.

The reasons for assuming equation (1) are that the form and coefficient values of the fault law in situ are not well known (indeed, they are to be found from analysis of field data), that the law describes a finite size patch with smoothly continuous dependence of stress on slip and position, and that the law allows instability to occur in a natural way for certain ranges of parameter values. However, the law contains no rate dependence, which in any case is insufficient by itself to produce instability, though it may modify conditions before and during instability, and no mechanism for postinstability healing of the fault in preparation for another instability. Similar bell-shaped constitutive laws have been employed in related instability models by *Stuart* [1979*b*], *Stuart and Mavko* [1979], and *Li and Rice* [1983].

Instability occurs when the resisting force of the patch decreases more rapidly with increasing τ^r than the force applied by the elastic surroundings. When this condition holds, static equilibrium cannot be maintained, and the fault slip jumps ahead owing to elastic rebound until forces are again in balance. Whether or not instability occurs depends on values of model parameters. Two limiting cases illustrate the range of behavior: Instability cannot occur if the rate of slip weakening is zero, $S/a_u \to 0$, and instability always occurs if the rate of

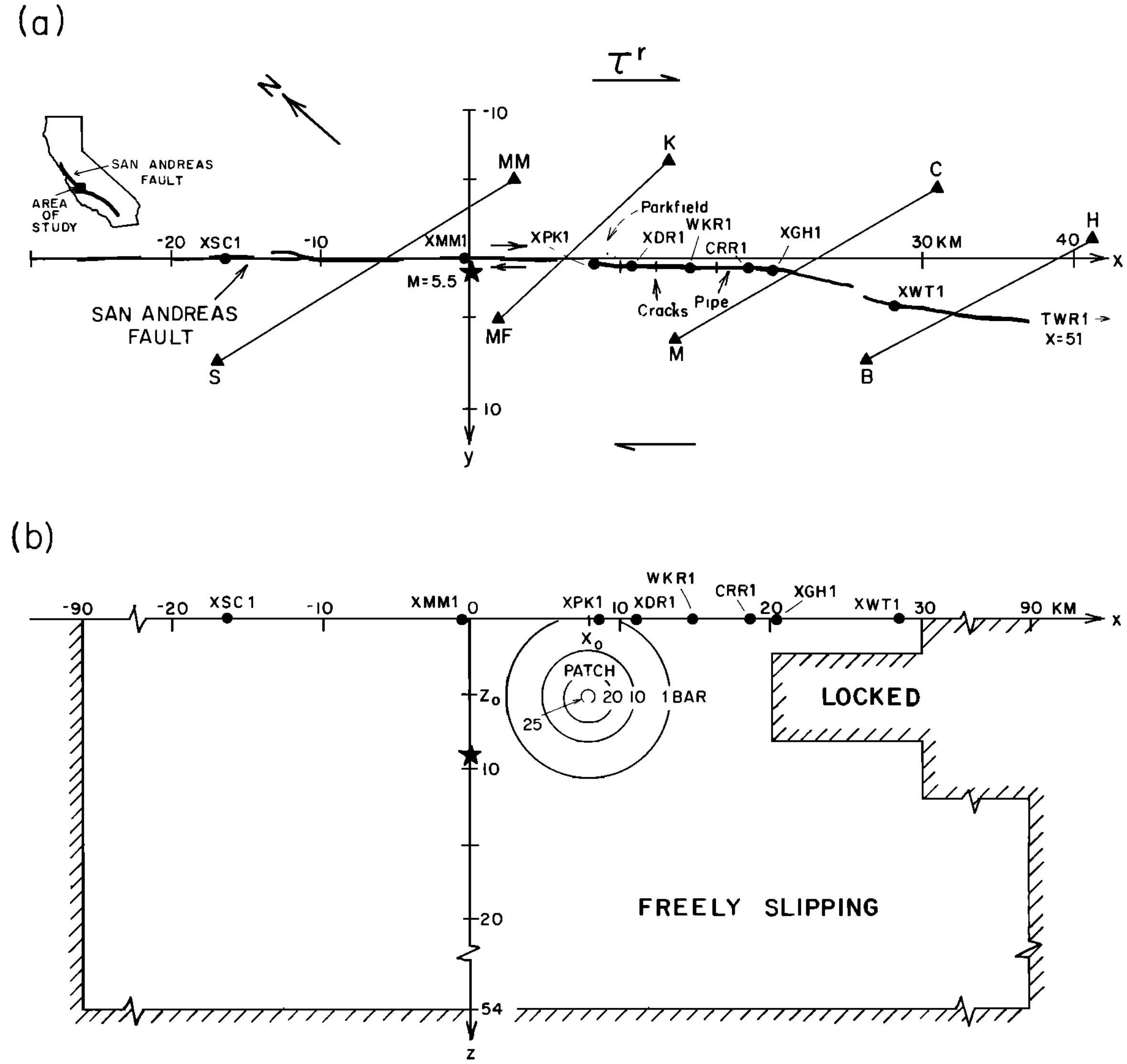

Fig. 3. (*a*) Map of the San Andreas fault trace near Parkfield. Dots are creepmeter locations. Triangles are locations of benchmarks at ends of trilateration lines. Star marks epicenter of $M_L = 5.5$ 1966 earthquake. $x - y$ axes are for model in Figure 3*b*. (*b*) Geometry of fault plane for the instability model. Patch location shown by contours of peak stress in bars. Star is location of the 1966 focus. Edge of locked fault indicated by hachures.

slip weakening is high enough, $S/a_u \rightarrow \infty$ (other model parameters finite). *Stuart* [1981] gives an elementary discussion of instability for the case of spacially uniform peak stress.

The actual model simulation involves finding the solution to a set of nonlinear equations expressing static equilibrium at the fault. For numerical solution of the governing equations, the fault is divided into rectangular cells of uniform slip. At each value of τ^r an iterative procedure (see the appendix) simultaneously adjusts cell slips until quasi-static equilibrium obtains at each cell centroid according to

$$\tau^r + \sum \tau^d - \tau^f = 0 \qquad (2)$$

where $\sum \tau^d$ is the sum of all dislocation stresses acting at the cell centroid, and τ^f is from (1). τ^f and each τ^d depend on cell slip. Ground surface deformation is computed from the cell slips and τ^r. τ^r and τ^d, like τ^f, are stress deviations with respect to the lower yield stress in (1), not total stresses.

The displacement and stress fields that are the solutions to (2) represent only part of the total fields in the earth. Some of the other parts, not modeled here, would be due to long-term slippage of the creeping fault north of Parkfield, earlier moderate earthquakes at Parkfield, and the 1857 earthquake. The displacement and stress fields due to the formation and later failure of the current patch may be thought of as perturbations to the fields from all other causes.

Model Parameters

For the model to be useful for prediction, the values of model parameters must be such that theoretical and observed curves of creep and trilateration data coincide for past data. The process of making the curves coincide is equivalent to estimating the parameter values. The parameters whose values can be estimated from available field data are x_0, z_0, $a_x = a_z$, S, a_u, and the three shallow boundaries of the locked lobe in Figure 3*b*. The eight model parameters are constrained by ten sets of data: nine creepmeter records and one trilateration line (MF-K). Theoretical curves for the other three trilateration lines in Figure 3*a* are essentially the same for all values of model parameters that satisfy the 10 sets of data. First we describe the method for estimating the parameter values, then we assess the agreement between theoretical results and observed data, and finally we determine the resolution of the model parameters.

If the instability model were sufficiently accurate, and the observations had smaller errors and were smoother functions of time, it might be possible to estimate the time, size, and location of future unstable slip from available creep and trilateration data alone. The small curvatures like those of the computed $u(\tau^r)$ traces would, in effect, constrain all model parameters plus the regional stress rate $\partial\tau^r/\partial t$, which sets the model time scale. However, such curvature is not recognizable in the measurements (Figures 4 and 5), and the data are adequately fit by straight lines, thus preventing the estimate of $\tau^r/\partial t$ and the earthquake time.

Until the field data become nonlinear, we are forced to make a provisional estimate of the earthquake time just to compare theory and observation. We get $\partial\tau^r/\partial t$ by matching two different values of τ^r in a model simulation to two values of t in the field data. One of the t values is from the earthquake recurrence interval. The matching is unambiguous because the model deformation history divides naturally into four successive stages corresponding to patch states. Thus values of τ^r and t at two stage boundaries of the simulation and of the field data fix $\partial\tau^r/\partial t$.

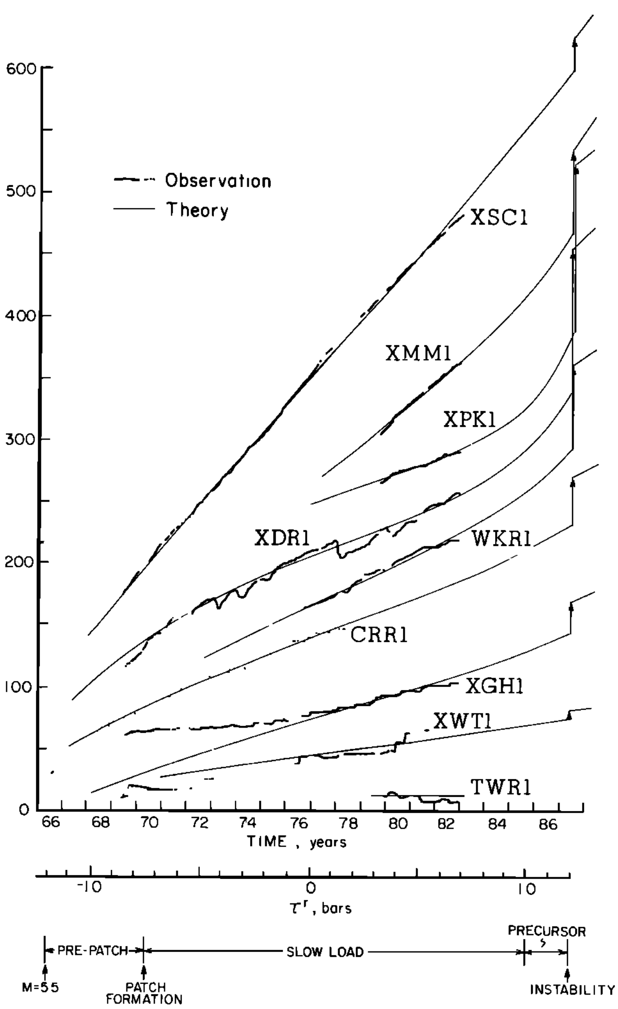

Fig. 4. Comparison of observed and theoretical fault creep at sites in Figure 3. Observation time scale, model τ^r, and model stages shown at bottom. Theoretical creep has been multiplied by 0.8 to compensate for underestimate of fault slip measured by creepmeters.

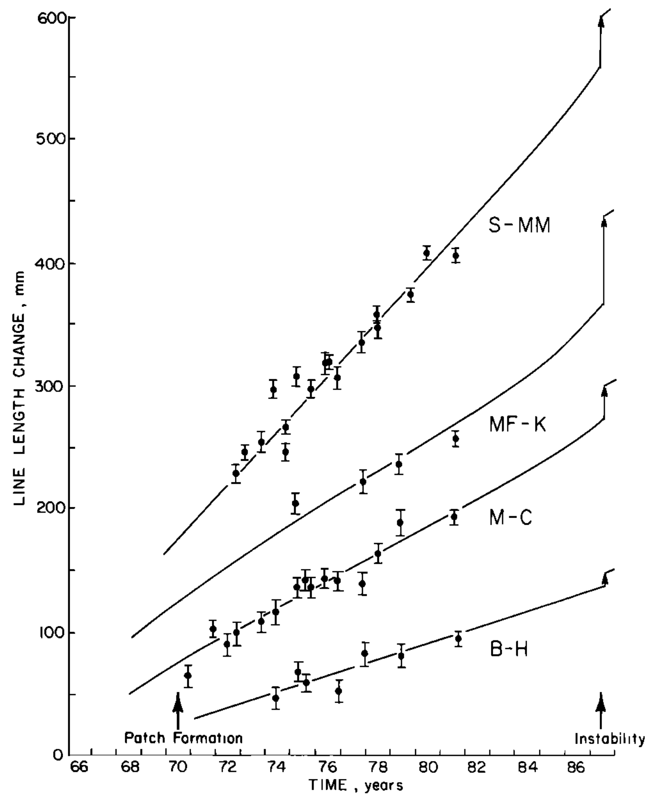

Fig. 5. Comparison of observed and theoretical length changes of trilateration lines in Figure 3a. Data are from *Slawson and Savage* [1983] and J. C. Savage (unpublished data, 1983). Error bars are 2 standard deviations. Line name abbreviations are S-MM, Shade-Mine Mountain; MF-K, Mid F-Kenger; M-C, Mason-Cotton; B-H, Bench-Hatch.

The model stages are (1) an interval of free slip before patch resistance, (2) slow loading of the patch, (3) precursory patch failure, and (4) instability. In the earth the prepatch stage spans the time between destruction of the old patch during the 1966 earthquake and the time of healing of the fault zone to form the current patch. The slow load and precursory stages are in effect from the time of patch healing to the earthquake. In the model, of course, the instability has zero duration, unlike an actual earthquake rupture.

The stress-slip law, equation (1), does not allow for healing of a previously failed patch, but the law's shape produces results in simulations that mimic healing. When fault slip is far out on the left tail of the Gaussian curve ($u \ll -a_u$), both shear stress and slope are small. For these values of fault slip the fault slides as if the patch were absent, producing model stage 1. As fault slip nears $-a_u$, shear stress and slope increase, and the patch begins to resist slippage. Model stages 1 and 2 would also result if a more general fault law which produced delayed healing after a prior instability were used, or if τ^f in (1) were arbitrarily replaced with $\tau^f = 0$ for a specified time interval representing stage 1. Since the details of patch healing are even more conjectural than the existence of a patch at Parkfield, equation (1) is used for simplicity.

The value of τ^r at the stage 1–stage 2 boundary is defined to be when the rate of increase of average fault stress $\bar{\tau}^f$ (equal to the average of τ^f at all cell centers) is maximum. Thus the boundary is the transition from the high rates of fault slip of stage 1 to the lower rates of stage 2. Values of τ^r at maximum curvature of individual $u(\tau^r)$ traces vary slightly from the value at maximum curvature of $\bar{\tau}^f(\tau^r)$. During most of stage 2, the slow load stage, slip near the patch center is negligible, and rates of ground surface displacement and of fault slip well outside the patch vary slowly with increasing τ^r. The patch area shrinks gradually, but the patch core remains intact. The start of the precursory stage is defined to be when $\bar{\tau}^f$ switches from increasing to decreasing, i.e., from $\partial\bar{\tau}^f/\partial\tau^r > 0$ to $\partial\bar{\tau}^f/\partial\tau^r < 0$. This stage is characterized by rapid but stable decline of average fault stress. The final stage is unstable fault slip, $\partial\bar{u}/\partial\tau^r \rightarrow \infty$. On curves of u versus τ^r, the instability appears as a jump of fault slip at constant τ^r.

In general it is misleading to call stage 3 a precursory stage, since patch failure could occur without instability. At Parkfield, however, the recurring moderate earthquakes, as well as the creep and trilateration data, imply that only unstable patch failure occurs. In instability models that contain pore fluid flow or viscoelastic deformation [e.g., *Rice and Rudnicki*, 1979; *Li and Rice*, 1983], the precursor stage is defined to be when fault slip is driven inevitably to instability by the rate-dependent mechanism, even when the regional forcing is held constant.

The start of the slow load stage in the field is the first time value used for finding $\partial\tau^r/\partial t$. Seismicity, fault creep, and trilateration data indicate that the slow load stage at Parkfield started about 1970 and continued through 1982. The patch at Parkfield must have reformed after the 1966 earthquake and its aftershocks but before the onset of nearly linear creep and trilateration trends starting about 1970. The time of aftershock cessation, extrapolated from the decreasing rate of aftershocks from June 1966 to January 1967 [*McEvilly et al.*, 1967; *Eaton et al.*, 1970], is about 1970. Reliable seismicity data for $M_L <$ 3 earthquakes from January 1967 through 1968 are unavailable. The current pattern of seismicity on the San Andreas fault at Parkfield (Figure 2) started about 1970 [*Buhr and Lindh*, 1982].

Three of the nine creepmeter records in Figure 4 have possible slope decreases starting about 1970. The data are from *Schulz et al.* [1982] except for CRR1 data 1966–1967, which are from *Smith and Wyss* [1968]. Creepmeter XSC1 has a hint of rate decrease in 1971, though the change is small as would be expected at a site so far from the patch, and comparable rate changes occur also after 1971. Similarly, the slope of XDR1 before 1971 is greater than the average slope of subsequent data. The reversals of the XDR1 trace may be due to seasonal transfer of slip from the fault strand spanned by the creepmeter to a nearby strand (R. O. Burford, personal communication, 1984). CRR1 data, which start in 1966, show a clear slope change about 1969. On the other hand, XGH1 shows a slope increase in 1975. The reason is unknown, but the irregular fault geometry and echelon offset near the instrument site may be factors. Finally, trilateration lines remained on trend after 1970 (Figure 5), though the large scatter would conceal small rate changes. Rates of trilateration lines M-C and others in the Parkfield area from 1966, postearthquake, to 1970 are generally greater than later rates [*Slawson and Savage*, 1983], as would occur if the patch were absent, but perhaps are instead due to different survey procedures [*Savage*, 1975]. All of these suggestive data support the patch having formed about 1970 and assign a time to the stage 1–stage 2 boundary of the model.

The second correspondence between τ^r and t needed for $\partial\tau^r/\partial t$ is set by tentatively assuming the earthquake time to be June 1987 using the earthquake recurrence interval. Thus the τ^r change between onset of the slow load stage and instability corresponds to the earthquake recurrence time minus the duration of the prepatch stage. The relation between model stages and time is shown at the bottom of Figure 4. The numerical value for $\partial\tau^r/\partial t$ is found after estimating values of model parameters. In a later section we outline a procedure for refining the $\partial\tau^r/\partial t$ estimate when, according to the theory, observations should depart from their recent, nearly linear trends.

An alternative to choosing a tentative earthquake time is to match the theoretical unstable slip to the inferred seismic slip of the 1966 earthquake. The disadvantage of this method is that the instability model may not accurately simulate seismic slip because of neglected inertia and rate-dependent processes, which would be most important near and during earthquake rupture. Also, the 1966 seismic slip itself is poorly known.

Values of model parameters are chosen by trial for best agreement between observed and theoretical fault creep and trilateration data, assuming that field data 1970–1982 represent part of the slow load stage of the model. It is convenient to split the eight parameters into two groups and estimate values for each group in turn. The first group contains the patch center location x_0 and z_0, patch radius $a_x = a_z$, the characteristic fault zone stiffness S/a_u, and the geometry of the locked lobe. The position of the lobe boundary at and below $z = 8$ km is assumed, since the data cannot resolve it. The crustal rigidity μ is assumed to be 3×10^{11} dyn/cm^2. Parameter values in the first group are determined by adjusting them one at a time until the agreement between simulated rates of fault creep and line lengthening, relative to the simulated creep rate at XSC1, and the corresponding relative rates of the field data do not improve. The unknown relative origins of the data do not affect the parameter estimates. The reason for matching ratios of rates is that they are independent of S and a_u individually (and thus $\partial\tau^r/\partial t$) as long as S/a_u is invariant. This is because mechanically similar boundary value problems are defined by the model geometry and the dimensionless rigidity $\mu' = (\mu/z_0)/(S/a_u)$, implying that the first group of parameters uniquely prescribes a dimensionless problem. After estimating the parameters of the first group, the parameters of the second group, S and a_u, are adjusted, while maintaining their ratio invariant, until the average computed rate for XSC1 matches the average observed rate for the years 1970 to 1982.

The results are given in Table 1. Column 1 lists the names of creepmeters and trilateration lines, and column 2 lists the observed rate obtained by fitting a least squares line to the data for the time intervals in column 3. The listed creep rates are 1.2 times higher than actually measured to compensate for the general underestimate of fault slip measured by creepmeters. The factor 1.2 is the nominal average ratio of fault slip measured by alinement arrays to slip measured by nearby creepmeters on the San Andreas fault in central California [*Burford and Harsh*, 1980; *Schulz et al.*, 1982]. Alinement array data are more accurate than creepmeter data because the arrays have longer baselines (about 100 m versus 10 m), and they generally agree with trilateration measurements using line lengths of about 1 to 3 km [*Lisowski and Prescott*, 1981].

Column 4 gives the observed rates and standard deviations relative to the observed rate of XSC1. The formula for the standard deviation of the relative rates, computed from the error propagation formula for uncorrelated errors, is $\sigma_i = \sqrt{2} \cdot \sigma\langle\dot{u}\rangle_i/\langle\dot{u}\rangle_{\mathrm{XSC1}}$, where $\langle\dot{u}\rangle_i/\langle\dot{u}_{\mathrm{XSC1}}\rangle$ is the measured rate of creepmeter or trilateration line i divided by the measured rate of XSC1. $\sigma = 0.1$ is the nominal standard deviation of the

TABLE 1. Comparison of Observed and Theoretical Rates of Fault Slip and Lengthening of Trilateration Lines

Observation Name	Observed $\langle \dot{u} \rangle$, mm/yr*	Time Interval	Observed $\langle \dot{u} \rangle / \langle \dot{u} \rangle_{XSC1}$	Theoretical $\langle \dot{u} \rangle / \langle \dot{u} \rangle_{XSC1}$	Theoretical $\langle \dot{u} \rangle$, mm/yr
XSC1	27.4 ± 3.8	1970–1982	1.00 ± 0.14	1.00	27.4
XMM1	21.4 ± 3.0	1979–1982	0.78 ± 0.11	0.73	20.0
XPK1	9.0 ± 1.3	1979–1982	0.33 ± 0.05	0.35	9.6
XDR1	10.3 ± 1.4	1970–1982	0.38 ± 0.05	0.37	10.1
WKR1	11.7 ± 1.6	1976–1982	0.43 ± 0.06	0.42	11.5
CRR1	10.5 ± 1.5	1970–1978	0.38 ± 0.05	0.34	9.3
XGH1	5.6 ± 0.8	1976–1982	0.21 ± 0.03	0.27	7.4
XWT1	4.5 ± 0.6	1970–1981	0.16 ± 0.02	0.12	3.3
TWR1	−2.8 ± 0.4	1979–1982	−0.10 ± 0.01	...	...
S-MM	20.6 ± 1.3	1972–1981	0.75 ± 0.09	0.79	21.6
MF-K	10.8 ± 4.1	1975–1981	0.40 ± 0.16	0.46	12.6
M-C	11.7 ± 1.2	1970–1981	0.43 ± 0.06	0.40	11.0
B-H	5.9 ± 2.1	1974–1981	0.27 ± 0.08	0.23	6.3

*Creepmeter rates have been multiplied by 1.2 for consistency with alinement array measurements.

ratios of alinement to creepmeter rates, with respect to the average of 1.2, and is a rough estimate of the accuracy of a creepmeter rate. Standard deviations of the least squares slopes of measured creep data are all less than 0.05 mm/yr and are therefore negligible.

Column 5 lists the theoretical relative rates resulting from the simulation using the best fit parameter values, which are given in columns 1 and 2 of Table 2. The computed relative rates are approximate average values for the middle section of the curves during the slow load stage. A comparison of columns 4 and 5 in Table 1 shows that theoretical rates are within one standard deviation of the observed rates for all observations except XGH1 and XWT1, which are more sensitive to changes of the lobe geometry than to changes of the best fit patch parameters. The theoretical slip for TWR1 is zero by assumption. Column 6 gives the unscaled theoretical rates.

Figure 4 shows the theoretical fault creep versus time curves superimposed on curves of measured creep. The overall agreement is good except for seasonal fluctuations, creep events (steplike jumps), and XGH1 before 1975. The agreement between theoretical and observed trilateration data, Figure 5, is also good, although the frequency and errors of the measurements are more permissive than those of creep data. Poorest agreement is for line MF-K, whose few data would seem to fit better a line of lower slope, but the data are still consistent with the theory because the standard deviation of the slope is 0.16 (Table 1, column 4). Merging the focal patch and the middle patch of Figure 2 into a single patch would decrease the theoretical rate for line MF-K. The combined patch would be a little more consistent with the seismicity distribution and would be preferred if it turns out that measured creep rates at XMM1 and XPK1 in Table 1 have an error that makes them systematically high.

The remaining uncertainty is the resolution of model parameters. The simplest way to estimate their resolution is to compute the changes of relative rates due to a perturbation of each parameter in turn. Columns 3, 4, and 5 in Table 2 show the results. As expected, the relative rates of fault slip at sites nearest the patch (XMM1, XPK1, and XDR1) are the most sensitive to perturbations of patch parameters. Increasing the depth of the patch center by 1 km causes a greater relative rate change than a 1-km perturbation to any other parameter. Alterations of the lobe geometry affect the slip rate at XGH1 and XWT1 more than at other sites. Individual perturbations of 2 km to the lobe top, left end, and top right end cause about 30% change in the relative rate at XGH1 or XWT1, but it is not possible to maintain a simple rectangular lobe shape and satisfy data at both XGH1 and XWT1 at once. No parameter perturbation causes relative rate changes greater than 0.03 to the trilateration lines. Overall, creepmeter data are 2 to 3 times as effective as trilateration data in constraining patch parameter values. In short, the observations are consistent with individual parameter perturbations of about 0.5 km to z_0; 1 km to x_0, a_x, and a_z; and 0.1 bar/mm to S/a_u.

A more thorough way to estimate the resolution of model

TABLE 2. Model Parameter Values and the Effect of Varying Each Value

Parameter Name	Parameter Value	Perturbation to Parameter Value	Most Sensitive Observation	Its Relative Rate Change
μ	3×10^{11} dyn/cm^2	...	...	...
x_0	8 km	−1 km	XDR1	0.05
z_0	5 km	1 km	XPK1	0.10
a_x	3 km	1 km	XMM1, XDR1	−0.05, −0.06
a_z	3 km	1 km	XPK1	−0.09
S/a_u	0.3 bar/mm	0.1 bar/mm	XPK1, XDR1	−0.04, −0.04
lobe left end, x	20 km	2 km	XGH1	0.08
lobe right end, x	30 km	2 km	XWT1	0.03
lobe top, z	2 km	2 km	XGH1	0.11
S	26 bars	...	...	...
a_u	86.7 mm	...	...	...
$\partial \tau^r / \partial t$	0.11 bar/yr	...	...	...

parameters is to find the subspace of all parameter values that gives theoretical relative rates within a standard deviation of observed relative rates. It is sufficient to consider only the three parameters z_0, $a_x = a_z$, and S/a_u because they can counteract one another to produce relative rates close to the best case rates in Table 1. x_0 is constrained to be between 7 and 9 km by creep rates at XPK1 and XDR1, which are low in comparison with the regional northwest-southeast variation along strike. The same two creep rates also constrain the patch shape a_x/a_z to be between about 0.4 and 2.0. The bottom end of a vertically elongated patch cannot be resolved by the data, and so the patch is perceived to be circular. A patch more than 2 times wide as tall violates the data.

The elliptically shaped envelopes in Figure 6 enclose parameter combinations for simulations whose relative rates do not differ by more than one standard deviation from observed relative rates. Each envelope is for a set of simulations at constant S/a_u, and each small dot represents one or more simulations for particular values of (z_0, $a_x = a_z$, S/a_u). The large dot represents the best fit case. There are no acceptable solutions for $S/a_u \leq 0.05$ bar/mm or $S/a_u \geq 0.8$ bar/mm. As shown by the two inclined straight lines, z_0 and a_x within envelopes are consistent with the additional requirements that the top edge of the patch be below the ground surface and the bottom edge be above the region of ductile deformation, starting at about 12-km depth.

The elongate shape of the envelopes implies that enlarging a patch compensates for increasing its depth. Big deep patches and small shallow patches will have similar variation of near-surface peak stresses and thus also similar configuration of their top edges. A similar argument accounts for the migration of the envelopes in a direction normal to the long axes of the envelopes when S/a_u changes. Lowering S/a_u is equivalent to making the surrounding half space less compliant by raising its rigidity. With a high rigidity the top edge of the patch must be broader and shallower to inhibit fault slip near XPK1 and XDR1 the same as when the rigidity is smaller.

For simulations represented by points inside the envelopes of Figure 6, the ratios of the durations of the precursor stages to the durations of the slow load stages are within 50% of the ratio for the best fit case. The relative rates of fault slip at the end of the precursor stage are within 40% of the best fit rates. High values of S/a_u are associated with short precursor stages and high preinstability slip rates, with the duration of the precursor stage varying from about 1 to 3 years.

In summary, the model is consistent with the data, except for two creepmeters far from the patch, when the patch radius is between 2.5 and 4.5 km, and the depth of the patch center is between 3 and 6 km. The best fit parameter values correspond to unstable patch failure, in agreement with the known occurrence of moderate earthquakes.

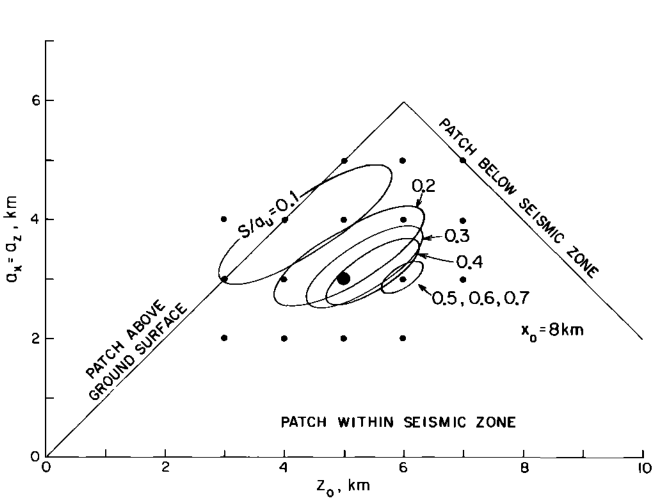

Fig. 6. Plot showing values of parameters z_0, $a_x = a_z$, and S/a_u that give theoretical relative rates within one standard deviation of observed relative rates. Envelopes enclose acceptable solutions having the same S/a_u. Sloping straight lines define the allowable depth interval containing the entire brittle patch. Small dots represent numerical simulations, and the large dot represents the best fit case in Table 2.

Fault Slip, Fault Stress, and Ground Uplift

During the slow load and precursory stages, there is a local minimum of slip rate on the fault plane near the patch center. With increasing τ^r the area of unfailed patch, defined by $u < 0$, shrinks, while at the same time the stress drop associated with failure of the patch rim increases. Starting near the end of the slow load stage and continuing through the precursor stage, the stress drop is large enough to create a circumferential band of high slip rate around the unfailed patch. This halo of high slip rate, a statically stable elastic rebound, is due to release of nearby elastic strain energy when the patch rim fails.

Figure 7a shows contours of fault slip rate $\partial u/\partial \tau^r$ on the fault plane when the patch is resisting overall fault slip most effectively, defined to be when the computed $\dot{u}_{XSC1}$ is minimum near the middle of the slow load stage. (To convert $\partial u/\partial \tau^r$ from millimeters per bar to millimeters per year, multiply by 0.11 bar/yr.) The dots mark the centers of the uniform slip dislocations used in the numerical solution. Slip rate is low at the patch center relative to the rate in surrounding areas. The shaded region, extending 10 km to the left of the patch center and to 12-km depth, encloses unfailed patch. The patch partially shields the fault between the patch center and the lobe from the stress concentration acting on the patch. At the end of the slow load stage, Figure 7b, the overall rate of fault slip has increased, but in the unfailed patch itself the slip rate remains low. An irregular region of high slip rate borders the reduced area of unfailed patch. At the end of the precursor stage and just before instability, Figure 7c, the slip rate around the patch has doubled, and the unfailed patch has collapsed to about 2-km radius. As in Figure 7b, the locus of maximum fault slip rate is at the lower left edge of the patch. The position of maximum fault slip acceleration, obtained from a higher-resolution simulation using τ^r increments of 0.01 bar instead of 0.05 bar, is marked by the square at 7-km depth in Figure 7c. This position is interpreted to be the analog of the earthquake focus because it is where stress waves would be generated first in a fully dynamic model.

Unstable fault slip is shown in Figure 7d. The maximum slip of 308 mm occurs about 2 km from the patch center, decreasing to about 50 mm at 10-km distance. Unstable slip is nonzero everywhere on the nonlocked fault plane because postinstability fault stress is essentially zero.

The evolution of shear stress on the fault plane reflects the increasing stress concentration on the decreasing patch area. Figures 8a, 8b, and 8c show fault stress for the same values of τ^r as in Figures 7a, 7b, and 7c. During maximum patch resistance to slippage, Figure 8a, the patch stress decreases from about 5 bars at the patch center to less than 0.1 bar at 6-km distance. At the end of the slow load stage, Figure 8b, stresses on the patch center have risen to 14 bars, and portions of the fault more distant than about 4 km have undergone a stress drop due to failure. Just before instability, Figure 8c, the maximum fault stress in the remaining patch is about 19 bars. Even

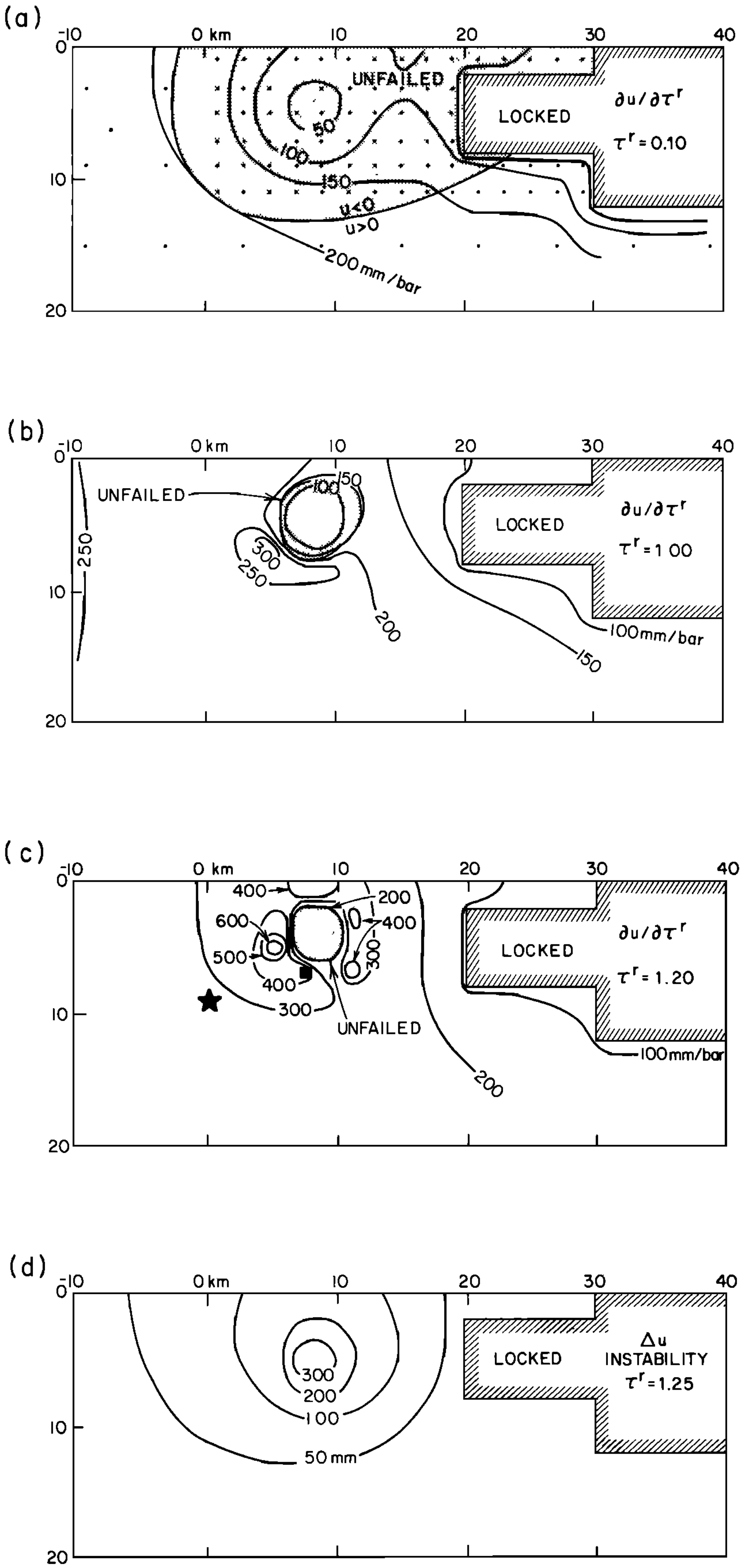

Fig. 7. Theoretical fault slip rate $\partial u/\partial \tau^r$ at (*a*) maximum patch resistance, during slow load stage, (*b*) end of slow load stage, and (*c*) end of precursory stage. Value of 100 mm/bar corresponds to 11 mm/yr. Unfailed patch, $u < 0$, is shaded. In Figure 7*c*, star is position of 1966 mainshock focus, and square is position of model focus. Theoretical slip during instability is shown in Figure 7*d*.

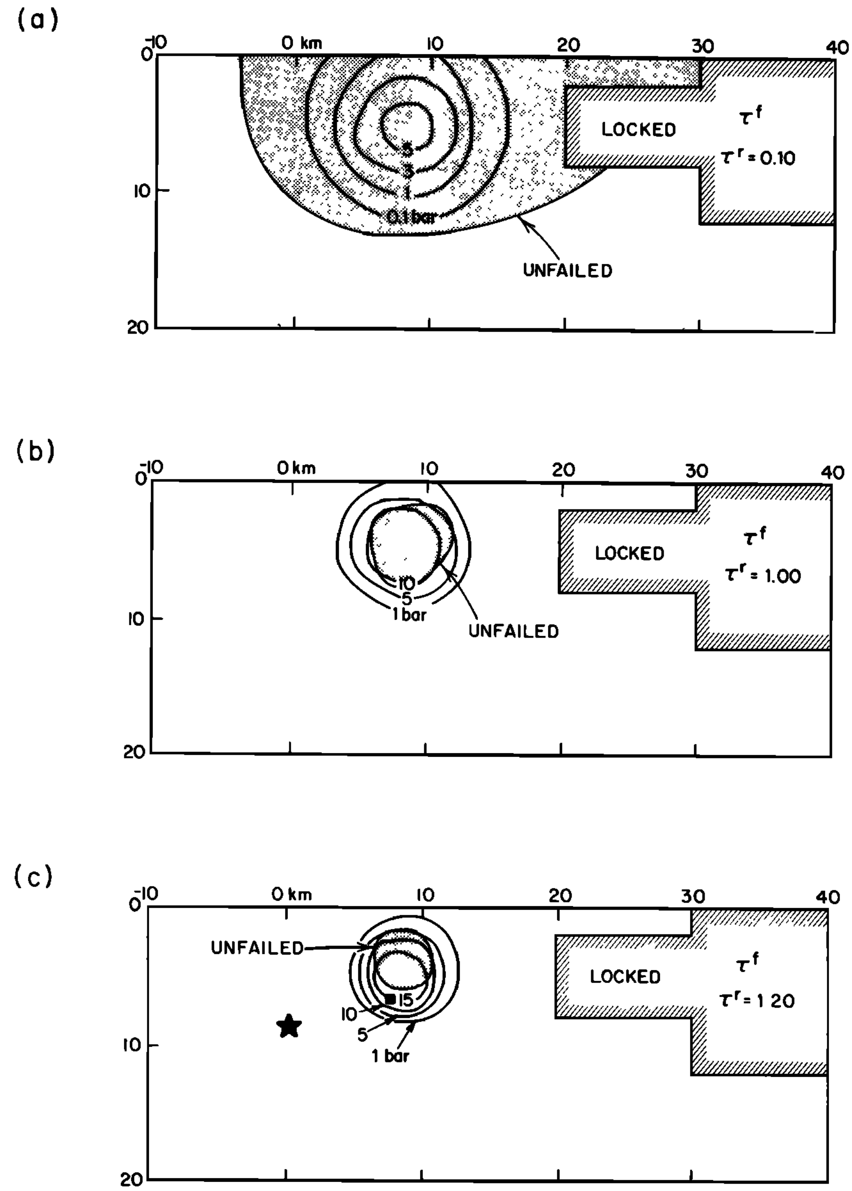

Fig. 8. Theoretical fault shear stress τ^f at (*a*) maximum patch resistance, (*b*) end of slow load stage, and (*c*) end of precursor stage. Unfailed patch is shaded. In Figure 8*c*, star is position of 1966 mainshock focus, and square is position of model focus. During instability, all stresses shown in Figure 8*c* drop to less than 0.01 bar.

though the largest value of shear stress occurs at this time, the average fault stress has been decreasing since the end of the slow load stage, Figure 8*b*. Stress contours in Figure 8*c* also closely approximate the stress drop during instability because all stresses after unstable slip are less than 0.01 bar. The sequence of fault stress maps, Figures 8*a*, 8*b*, and 8*c*, illustrates that instability is a property of the mechanical system consisting of the interacting fault and elastic half space, rather than of particular stress or strength values at any special location on the fault. At the onset of instability, areas of the fault far from the patch edge have already failed, areas just outside the patch edge are in the process of failure, and areas inside the edge must undergo an initial stress increase during instability before their final stress decrease.

Seismic slip and stress drop during the 1966 earthquake provide an independent check of the model. In the model the coseismic slip averaged over the entire unlocked fault is 1.7 cm with a maximum slip of 31 cm near the patch center. The seismic moment (the product of μ, fault area, and average fault slip) is 4.7×10^{25} dyn cm. The maximum stress drop is 19 bars, and the average stress drop is 0.05 bar. By comparison, dynamic models of the 1966 earthquake [*Archuleta and Day*, 1980] indicate an average coseismic slip of 43 cm, a maximum of 60 cm, an average stress drop of 25 bars, and a seismic moment of 2.5×10^{25} dyn cm. *Tsai and Aki* [1969] infer a moment of 1.5×10^{25} dyn cm from the analysis of surface waves. Averaging instability model results over a smaller fault area approximately the size of the 1966 aftershock zone [*Eaton et al.*, 1970; *Lindh and Boore*, 1981] (300 km^2 for the unlocked fault area $x > 0$ km, $z < 12$ km) gives average slip of 9.2 cm, average stress drop of 1.6 bars, and moment of 0.8×10^{25} dyn cm. Theoretical slip and stress changes would be larger if a few kilometers of the lobe end failed during instability, and the results of some dynamic models [*Archuleta and Day*, 1980] support seismic slippage in the lobe end.

The model earthquake focus and the focus of the 1966 event do not agree well. The 1966 focus [*Lindh et al.*, 1983] is about 7 km northwest of and 2 km deeper than the computed focus

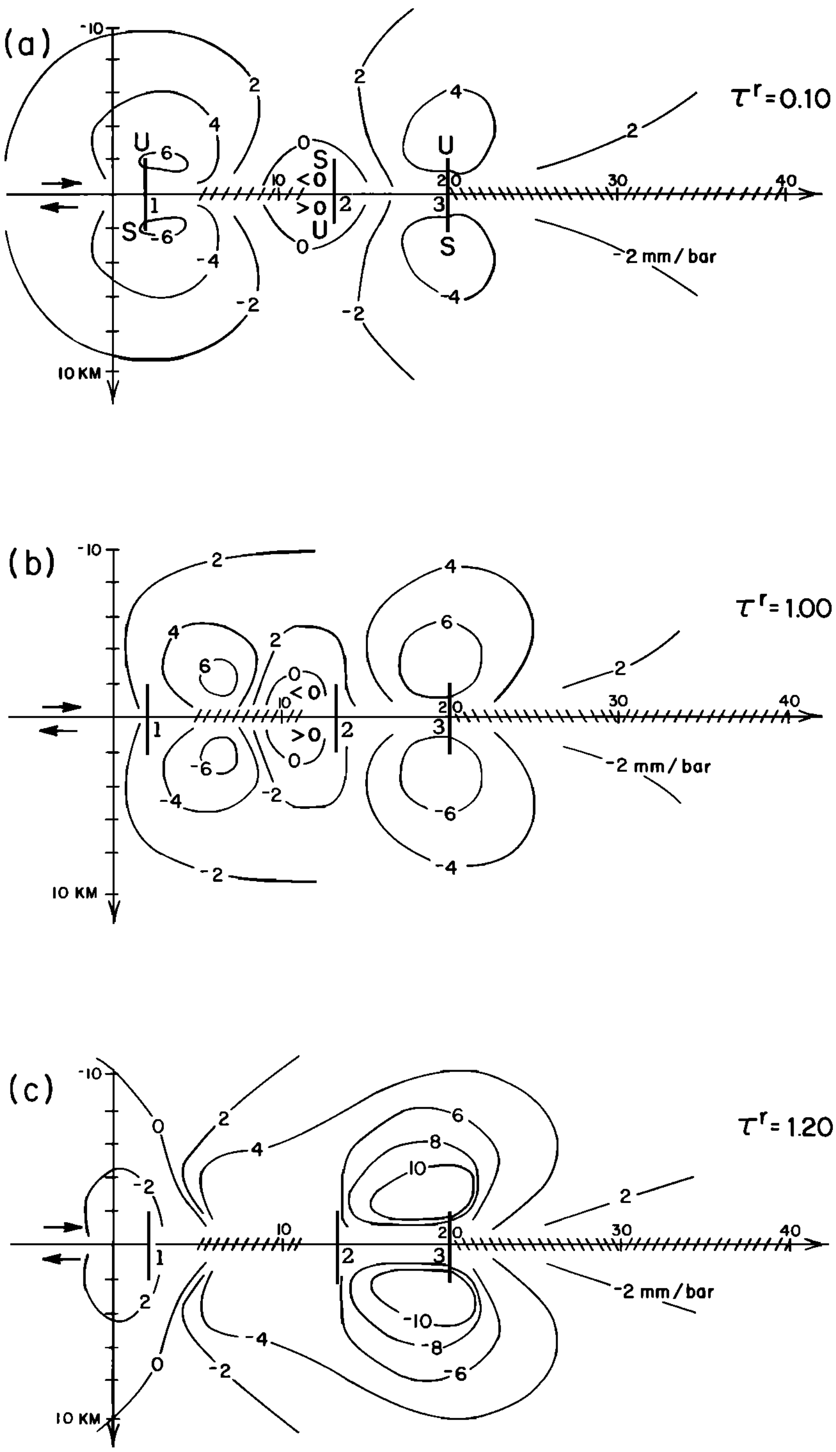

Fig. 9. Theoretical uplift rate at the ground surface at (*a*) maximum patch resistance, (*b*) end of slow load stage, and (*c*) end of precursor stage. Value of 10 mm/bar corresponds to 1.1 mm/yr. The hachured segment of the fault trace near $x = 10$ km is the projection of the patch. The hachured segments between $x = 20$ and 30 km and $x = 30$ and 40 km are projections of the lobe top. U and S mark endpoints of hypothetical level lines 1, 2, and 3.

(Figure 7*c*). The discrepancy suggests that the model should contain another, but smaller, strain-softening patch near the actual focus (cf. Figure 2). The creep and trilateration data cannot resolve such a patch, however. The small patch may be related to dislocation pileup at the 5° mapped bend in the San Andreas fault near XMM1.

The changing patch resistance and size cause a distinctive pattern of ground surface uplift and subsidence. At the time of greatest patch resistance, Figure 9*a*, loci of maximum uplift and subsidence rates are at positions *U* and *S*, respectively, and hypothetical level lines 1, 2, and 3 crossing the fault trace tilt down toward *S*. At the end of the slow load stage, Figure 9*b*, the tilt rate of line 3 increases. The tilt rate of line 2 has changed sign because nearby ground that was formerly rising now sinks, and formerly sinking ground rises. The tilt rate of line 1 also reverses, but not until midway into the precursor stage. At the end of the precursor stage, Figure 9*c*, the maximum tilt deviations from the extrapolated earlier trends are about 0.5 microradian, an amount near the limit of detectability by current survey methods. The instability model allows only strike-slip motion on the fault, but a more general model would produce a small amount of dip-slip motion, which would cause arbitrarily large tilting of sufficiently short level lines crossing the vertical step at the fault plane.

Physically, the uplift pattern during the slow load stage is due to pileup of vertical edge dislocations against the left and right sides of the patch and against the left end of the locked lobe. During the slow load stage, the accumulating, rightward flowing dislocations cause uplift maxima and mimima near the ends of lines 1 and 3, while leftward flowing dislocations create the opposite pattern near the ends of line 2. Later, when the patch is weakening and shrinking during the precursor stage, the dislocations piled up against the patch partly coalesce and annihilate, and the remaining dislocations accumulate at the lobe end.

EARTHQUAKE FORECAST

According to the theory, the prominent rate changes of the precursory stage should start about 2 years before the next moderate earthquake (cf. Figures 4 and 5). All fault creep rates should increase, but the rates of XPK1 and XDR1 should be greatest and easily detectable within the data scatter about a year before the earthquake. This result is consistent with two observations suggesting accelerated fault slip before the 1966 earthquake. Fresh-appearing ground cracks, probably less than a month old, were observed near XDR1 11 days before the mainshock [*Allen and Smith*, 1966], and a partly buried pipe near CRR1 broke 9 hours before [*Yerkes and Castle*, 1967] (Figure 3*a*). The model also predicts that the four trilateration lines will have rate changes. Line MF-K, Figure 5, should have the greatest change, but its rate increase would probably be undetectable before the earthquake because of the data scatter. In the model the four trilateration lines show a precursory rate increase, but certain other lines with different locations and orientations show a rate reversal.

It may be possible to relate other precursory phenomena to the instability model by adding the appropriate physical theory. For example, seismicity migrations might accompany shrinkage of the patch. Alterations in the earth's magnetic field could result from preinstability stress changes distorting piezomagnetic rock. Both the depth to the water table and the rate of soil gas emanation may change because of the time-dependent dilatation.

If data acquired between now and the time of the earthquake are still consistent with the model, they may increase the accuracy and precision of the estimated earthquake time. Significant nonlinearity in creep versus time curves, for example, will provide an independent estimate of $\partial\tau^r/\partial t$, which so far has required that the earthquake time be assumed. New data may also provide improved estimates for values of patch parameters. Several scenarios are possible. One is that the values of $\partial\tau^r/\partial t$ and patch parameters in Table 2 are accurate but imprecise. That is, the numerical values are nearly correct, but the error bars are large. Then the new data will follow the theoretical curves in Figures 4 and 5, but the resolution of the parameter values and the earthquake time will increase. In other words, the envelopes of acceptable solutions in Figure 6 will shrink. Another scenario is that the new data will still be consistent with the preliminary values of the first group of patch parameters, but that $\partial\tau^r/\partial t$ will differ from the Table 2 value. In this case, the theoretical curves will need to be stretched or compressed along the time axis until theory and observation agree. A third possibility is that the model is physically correct, but all parameter values are wrong. Finally, the model may be so inaccurate that theoretical and observed curves cannot be made to coincide by any combination of parameter values inside the envelopes of Figure 6.

Some model deficiencies might be the failure to account for pore fluid flow or time- and pressure-dependent fault properties. Other deficiencies could be that the regional stress rate changes with time, or that the magnitude and direction of principal regional stresses differ from simple shear. These differences could be caused by slip on nearby faults, for example, faulting related to the Coalinga earthquakes in May 1983 about 40 km north of Parkfield [*Borcherdt*, 1983]. Also, the model may need modification to include the fault bend near the epicenter, and the fault bends and offset near the XGH1 creepmeter.

CONCLUSIONS

We have outlined a procedure for using an earthquake instability model and repeated geodetic measurements to attempt an earthquake forecast. The procedure differs from other prediction methods, such as recognizing trends in data or assuming failure at a critical stress level, by using a self-contained instability model that simulates both preseismic and coseismic faulting in a natural way. In short, physical theory supplies a family of curves, and the field data select the member curves whose continuation into the future constitutes a prediction. Model inaccuracy and resolving power of the data determine the uncertainty of the selected curves and hence the uncertainty of the earthquake time.

In application to the pending moderate earthquake at Parkfield, the model and available field data are in good agreement overall. The near linearity of the field data imply large uncertainty of certain model parameters and of the earthquake time, but the model predicts departures from linearity before the earthquake. If observed, the preearthquake nonlinearity may increase the precision of the model parameters and the earthquake time. Future data will indicate the accuracy of the strain-softening patch model, and whether it needs modification for a more complicated fault law, such as the one suggested by *Dieterich* [1979], or inclusion of viscoelastic deformation of the underlying mantle, as suggested by *Li and Rice* [1983]. Nonetheless, some form of accelerating fault slip occurs in all instability models and is to be expected at Parkfield.

APPENDIX: NUMERICAL SOLUTION

For numerical solution of the boundary value problem, the continuous slip $u(x, z, \tau^r)$ of the nonlocked fault is approximated by uniform slip in n cells bounded by rectangular dislocation loops. For each value of the regional stress given by $\tau^r = \tau_0{}^r + m\Delta\tau^r$, where $\tau_0{}^r$ is the initial stress, m is the number of the time step, and $\Delta\tau^r$ is the stress increment at each time step, we seek an approximate solution u_i to the set of n equations

$$\tau^r + \sum_{j=1}^{m} \tau_i{}^d(u_j) - \tau_i{}^f(u_i) = 0 \qquad i = 1, n \tag{A1}$$

Each of the n equations in (A1) is the condition for shear stress equilibrium at a cell centroid. The second term is the sum of all dislocation stresses acting on cell i, including the self stress ($i = j$). Dislocation stresses are obtained from analytic solutions given by *Chinnery* [1963]. The third term, the resisting stress from the fault stress-slip law (1), makes equations (A1) nonlinear.

An initial guess of u_i, when inserted into the left side of (A1), generally gives nonzero departures from equilibrium, say $\Delta\tau_i$. In the solution algorithm, each u_i is improved by adding Δu_i calculated according to

$$\Delta u_i = \frac{\Delta\tau_i}{\partial\tau_i^f/\partial u_i - \partial\tau_i^d/\partial u_i} \qquad \text{(A2)}$$

In the denominator of (A2), $\partial\tau_i^f/\partial u_i$ is the analytically determined slope of the fault law at the current u_i, and $\partial\tau_i^d/\partial u_i$ is the analytically determined self stress per unit slip. If the overall departure from equilibrium $e = (\sum\Delta\tau_i^2)^{1/2}$ is greater than an acceptable value e_m, all $\Delta\tau_i$ are recalculated from (A1) and the new values of u_i, and then u_i are improved again with (A2). Essentially, (A2) estimates Δu_i using the stress nonequilibrium and stiffnesses of the fault law and dislocation. The advantages of (A2) are that it is simple; it finds solutions near and at instability without modification, despite the opportunity for singularity in the right side; and it has no adjustable parameters to alter the convergence rate. Ground surface displacements, from which length changes of trilateration lines are easily calculated, are from analytic solutions [*Chinnery*, 1963] using u_i, and the half space deformation due to τ^r alone.

In all simulations the width of the 119 nearly equant cells varies from 2 km near the patch center to 18 km at greater distances. The regional stress step is $\Delta\tau^r = 0.05$ bar, and the solution error e_m is 0.001 bar.

Acknowledgments. Research by W.D.S. was supported in part by National Science Foundation grant EAR-8018800. We thank W. H. Bakun and R. O. Burford for comments and J. C. Savage and S. S. Schulz for unpublished data.

REFERENCES

Allen, C. R., and S. W. Smith, Parkfield earthquakes of June 27–29, 1966, Monterey and San Luis Obispo counties, California—Preliminary report, *Bull. Seismol. Soc. Am.*, *56*, 966–967, 1966.

Archuleta, R. J., and S. M. Day, Dynamic rupture in a layered medium: The 1966 Parkfield earthquake, *Bull. Seismol. Soc. Am.*, *70*, 671–689, 1980.

Bakun, W. H., and T. V. McEvilly, Earthquakes near Parkfield, California: Comparing the 1934 and 1966 sequences, *Science*, *205*, 1375–1377, 1979.

Bakun, W. H., and T. V. McEvilly, *P*-wave spectra for M_L 5 foreshocks, aftershocks, and isolated earthquakes near Parkfield, California, *Bull. Seismol. Soc. Am.*, *71*, 423–436, 1981.

Bakun, W. H., and T. V. McEvilly, Recurrence models and Parkfield, California, earthquakes, *J. Geophys. Res.*, *89*, 3051–3058, 1984.

Borcherdt, R. D., The Coalinga earthquake sequence commencing May 2, 1983, *U.S. Geol. Surv. Open File Rep.*, *83-511*, 1983.

Brown, R. D., Map showing recently active breaks along the San Andreas fault between the northern Gabilan Range and Cholame Valley, California, *Map I-575*, U.S. Geol. Surv., Washington, D. C., 1970.

Buhr, G. S., and A. G. Lindh, Seismicity of the Parkfield, California region 1969 to 1979, *U.S. Geol. Surv. Open File Rep.*, *82-205*, 1982.

Burford, R. O., and P. W. Harsh, Slip on the San Andreas fault in central California from alignment array surveys, *Bull. Seismol. Soc. Am.*, *70*, 1233–1261, 1980.

Chinnery, M. A., The stress changes that accompany strike-slip faulting, *Bull. Seismol. Soc. Am.*, *53*, 921–932, 1963.

Dieterich, J. H., Modeling of rock friction, 2, Simulation of preseismic slip, *J. Geophys. Res.*, *84*, 2169–2175, 1979.

Eaton, J. P., M. E. O'Neill, and J. N. Murdock, Aftershocks of the 1966 Parkfield-Cholame, California earthquake: A detailed study, *Bull. Seismol. Soc. Am.*, *60*, 1151–1197, 1970.

Jaeger, J. C., and N. G. W. Cook, *Fundamentals of Rock Mechanics*, 3rd ed., Chapman and Hall, London, 1979.

Li, V. C., and J. R. Rice, Preseismic rupture progression and great earthquake instabilities at plate boundaries, *J. Geophys. Res.*, *88*, 4231–4246, 1983.

Lindh, A. G., and D. M. Boore, Control of rupture by fault geometry during the 1966 Parkfield earthquake, *Bull. Seismol. Soc. Am.*, *71*, 95–116, 1981.

Lindh, A. G., M. E. O'Neill, W. H. Bakun, and D. B. Reneau, Seismicity patterns near Parkfield, California (abstract), *Earthquake Notes*, *54*, 61–62, 1983.

Lisowski, M., and W. H. Prescott, Short-range distance measurements along the San Andreas fault system in central California, 1975 to 1979, *Bull. Seismol. Soc. Am.*, *71*, 1607–1624, 1981.

McEvilly, T. V., W. H. Bakun, and K. B. Casaday, The Parkfield, California earthquakes of 1966, *Bull. Seismol. Soc. Am.*, *57*, 1221–1224, 1967.

Rice, J. R., The mechanics of earthquake rupture, in *Physics of the Earth's Interior*, edited by A. M. Dziewonski and E. Boschi, pp. 555–649, Italian Physical Society/North-Holland, Amsterdam, 1980.

Rice, J. R., and J. W. Rudnicki, Earthquake precursory effects due to pore fluid stabilization of a weakening fault zone, *J. Geophys. Res.*, *84*, 2177–2193, 1979.

Savage, J. C., A possible bias in the California state geodimeter data, *J. Geophys. Res.*, *78*, 4078–4088, 1975.

Schulz, S. S., G. M. Mavko, R. O. Burford, and W. D. Stuart, Long-term fault creep observations in central California, *J. Geophys. Res.*, *87*, 6977–6982, 1982.

Sieh, K. E., Slip along the San Andreas fault associated with the great 1857 earthquake, *Bull. Seismol. Soc. Am.*, *68*, 1421–1448, 1978.

Slawson, W. F., and J. C. Savage, Deformation near the junction of the creeping and locked segments of the San Andreas fault, Cholame Valley, California (1970–1980), *Bull. Seismol. Soc. Am.*, *73*, 1407–1414, 1983.

Smith, S. W., and M. Wyss, Displacement on the San Andreas fault subsequent to the 1966 Parkfield earthquake, *Bull. Seismol. Soc. Am.*, *58*, 1955–1973, 1968.

Stuart, W. D., Quasi-static earthquake mechanics, *Rev. Geophys. Space Phys.*, *17*, 1115–1120, 1979*a*.

Stuart, W. D., Strain-softening instability model for the San Fernando earthquake, *Science*, *203*, 907–910, 1979*b*.

Stuart, W. D., Stiffness method for anticipating earthquakes, *Bull. Seismol. Soc. Am.*, *71*, 363–370, 1981.

Stuart, W. D., and G. M. Mavko, Earthquake instability on a strike-slip fault, *J. Geophys. Res.*, *84*, 2153–2160, 1979.

Tsai, Y.-B., and K. Aki, Simultaneous determination of the seismic moment and attenuation of seismic surface waves, *Bull. Seismol. Soc. Am.*, *59*, 275–287, 1969.

Wesson, R. L., R. O. Burford, and W. L. Ellsworth, Relationship between seismicity, fault creep and crustal loading along the central San Andreas fault, *Stanford Univ. Publ. Geol. Sci.*, *13*, 303–321, 1973.

Yerkes, R. F., and R. O. Castle, The Parkfield-Cholame, California earthquakes of June–August 1966, *U.S. Geol. Surv. Prof. Pap.*, *579*, 40–52, 1967.

R. J. Archuleta, Department of Geological Sciences, University of California, Santa Barbara, CA 93106.

A. G. Lindh, U.S. Geological Survey, 345 Middlefield Road, Menlo Park, CA 94025.

W. D. Stuart, U.S. Geological Survey, 525 South Wilson Avenue, Pasadena, CA 91106.

(Received February 1, 1984;
revised August 24, 1984;
accepted September 14, 1984.)